IEEE Access
Multidisciplinary | Rapid Review | Open Access Journal

Received 30 November 2023, accepted 20 December 2023, date of publication 25 December 2023,
date of current version 11 January 2024.

Digital Object Identifier 10.1109/ACCESS.2023.3347344

RESEARCH ARTICLE

Methods for Detection and Measurement of Potential Broncho-Arterial Pairs in Chest Computed Tomography Scans of Children

ABHIJITH REDDY BEERAVOLU[1], SAMI AZAM[1], MIRJAM JONKMAN[1], (Member, IEEE), I. BRENT MASTERS[2], RAHUL J. THOMAS[2,4], ANNE B. CHANG[2,3,4], GABRIELLE B. MCCALLUM[3], AND FRISO DE BOER[1]

[1]Faculty of Science and Technology, Charles Darwin University, Casuarina, NT 0810, Australia
[2]Department of Respiratory and Sleep Medicine, Queensland Children's Hospital, Brisbane, QLD 4101, Australia
[3]Child Health Division, Menzies School of Health Research at Darwin, Charles Darwin University, Darwin, NT 0909, Australia
[4]Australia Centre for Health Services Innovation, Queensland University of Technology, Brisbane, QLD 4000, Australia

Corresponding author: Abhijith Reddy Beeravolu (abhijith.beeravolu@cdu.edu.au)

This work involved human subjects or animals in its research. Approval of all ethical and experimental procedures and protocols was granted by the Human Research Ethics Committee (HREC), Menzies School of Health Research under Approval No. HREC-07/63.

ABSTRACT Bronchiectasis, one of the most neglected chronic lung conditions, has a high individual disease burden and economic cost and causes poor quality of life in children/adolescents and adults. Advances in image quality and a dramatic reduction in acquisition times, multiple high-resolution chest tomography (HRCT) acquisitions, and reconstructions of the lung have resulted in accurate categorization and determination of the extent of lung parenchyma and airway abnormality. For bronchiectasis, the diagnosis is confirmed using the key feature of abnormally increased broncho-arterial (B.A.) ratio (BAR), with or without other abnormalities, e.g., bronchial wall thickening, lack of bronchial tapering, and mucus plugging. Most of these features require shape analysis of the airway and artery regions to perform various assessments that can have inter-rater variability and are time-consuming. This challenge is amplified in pediatric patients due to age-related anatomical variations. The anatomical differences and variations in airway structures between Infants, Early Childhood, and middle Childhood can impact how the images can be processed and analyzed. To address this, we proposed two novel image-processing methods to detect and measure the B.A. pairs. The first method uses an optimized connected component labelling (CCL) algorithm to construct bounding boxes around the objects (airway, artery) and extract the regions of interest (ROIs) for potential B.A. pairs. The second method allows us to calculate 4 or 6 diameters for each object in the ROIs and use their mean value as the final diameter, demonstrating agreement with manual readings. Evaluating against a diverse set of HRCT scans from various categories validates the significance and practical utility of our proposed methods in detecting and measuring the disjointed B.A. pairs to assess increased BAR.

INDEX TERMS Airway, artery, broncho-arterial ratio, bronchiectasis, connected components, HRCT scans, pediatrics.

I. INTRODUCTION

Bronchiectasis in children is defined as a clinical syndrome of recurrent or persistent ($\geq$3) episodes of chronic (> four weeks) wet/productive cough, in combination with abnormal bronchial dilatation on chest computed tomography (C.T.) scans [1], [2]. Bronchiectasis is regarded as a heterogenous chronic pulmonary disorder. Although there are similarities between pediatric and adult bronchiectasis [1], multiple risks and etiologic factors differ between age groups [2], [3]. Identifying the factors contributing to the severity of bronchiectasis can help define various 'treatable traits' [2],

The associate editor coordinating the review of this manuscript and approving it for publication was Yongjie Li.

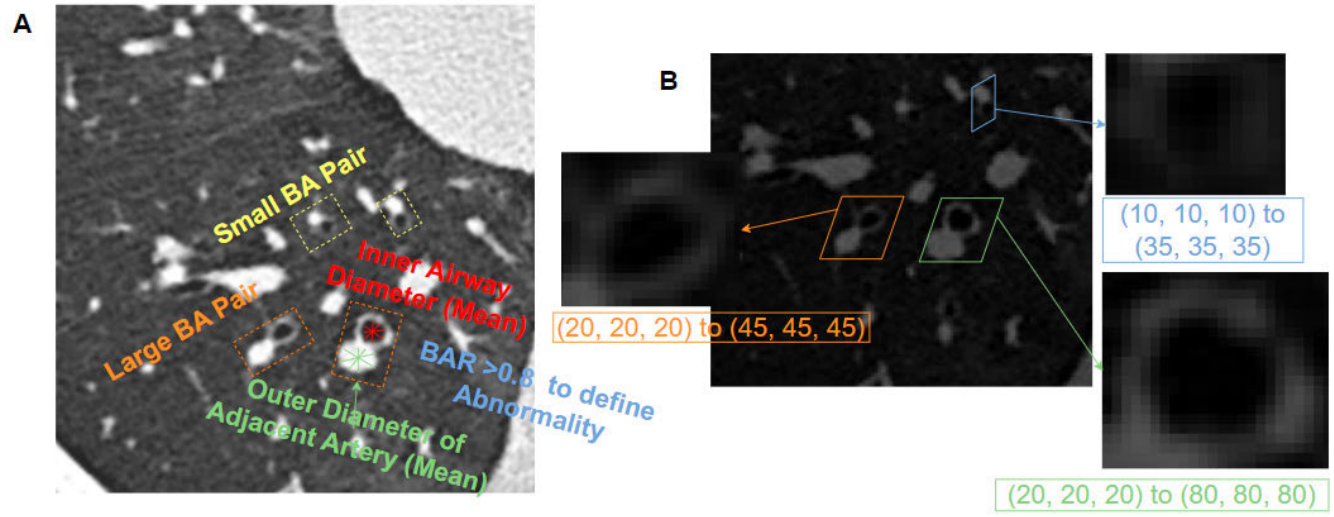

FIGURE 1. A thin section C.T. scan (HRCT) slice (0.67 mm) of a subject obtained from the right side of the lung at window width of 1500 HU and window level of -500 HU shows multiple Broncho-Arterial (B.A.) pairs (small-to-large); (B): The pixel intensity ranges (RGB) for airway wall of different B.A. pairs on a Grayscale DICOM slice.

[4], aiding clinicians in achieving a cure for at least a subset of children [2], [7]. Current clinical management guidelines for bronchiectasis are primarily based on adult data. Still, in recent years, clinicians have emphasized the need to conduct clinical research separately for children and adolescents [7], [20].

Bronchiectasis is confirmed radiographically using chest C.T. scan feature of increased B.A. ratio (BAR). It is often accompanied by other features, e.g., bronchial wall thickening, lack of bronchial tapering, and mucus plugging [2]. A high-resolution C.T. scan (HRCT) allows assessment of airway abnormality and severity of bronchiectasis from cylindrical (mild) to varicose, then cystic (severe) well-accepted severity markers are part of various radiographically based bronchiectasis scales [6].

Manual inspection of the available C.T. scans reveals that younger children generally have smaller airways than older children and adults. As children grow, their airways also become larger to accommodate the increased airflow demands associated with physical development. Careful evaluation and validation are required to detect B.A. pairs in HRCT scans of children of various ages. Therefore, we created three sets of full-length HRCT scans for different age groups: Infants (under two years), Early Childhood (2-6 years), and Middle Childhood (6-12 years). Working on these sets allowed us to check the differences between the required image processing parameters, validate the methods against many full-length scans, and prove the significance of the proposed methods for real-life scenarios.

A. BA PAIRS, BAR, & THE NEED FOR AUTOMATED SYSTEMS

The B.A. pairs in an HRCT scan can appear in various sizes, shapes (irregular), forms, and red, green, and blue (RGB) intensities. They can be large, medium, or small and appear in discrete pairs or accompanied by pulmonary veins, depending on the broncho-pulmonary segment and lobe they are situated in (Fig. 1A). Similarly, the RGB intensities of the airway walls can also differ based on their location (Fig. 1B). These are some of the essential aspects to keep in mind while developing a fully automated system for detecting potential B.A. pairs in HRCT scans.

The upper limit for the *normal* BAR in children was found to be 0.76. Thus, current guidelines recommend using a lower cutoff of >0.8 to define *abnormality in children* [2], [7], [8]. However, there is ongoing debate and different opinions on how B.A. ratios should be defined and determined. When determining BAR, some clinicians prefer to use the outer airway diameter [14]. However, the ERS pediatric guidelines [7] recommend using the inner airway diameter for the BAR, but this was a conditional recommendation due to limited evidence [7]. More studies on the prevalence of bronchiectasis in children are required; however, manually inspecting B.A. pairs in HRCT scans of various age groups can take a long time, limiting the scope of experimentation. And when there are no clinical symptoms present, a BAR $>$ 0.8 for a single B.A. pair may not always indicate abnormality (increased BAR) in children, similar to how a BAR larger than 1 does not always reveal the presence of bronchiectasis in adults [15]. We need image processing/machine learning methods for detecting and calculating the ratios for most B.A. pairs. The methods can allow the researchers to classify the B.A. pairs according to their segment/sub-segments and provide comprehensive airway tree evaluations and severity scores for optimal patient management.

Since most B.A. pairs in an HRCT scan have irregular shapes (both the bronchus and the artery), measuring inner airway and outer artery diameters with just one diameter (like for a circle) is insufficient. Clinicians have used [15] electronic calipers to measure two diameters

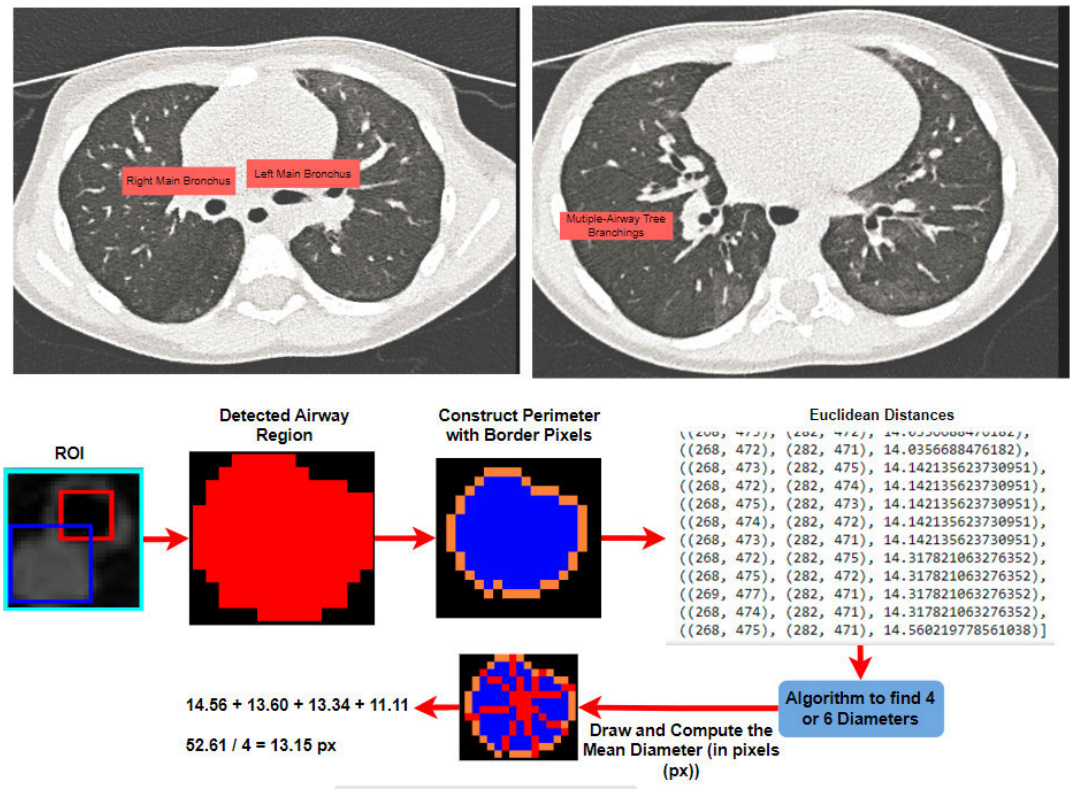

FIGURE 2. Airway tree branching and constructing perimeter with inner airway border pixels and measuring the Euclidean distance between all the coordinates to find 4 or 6 diameters and their mean.

(maximum and minimum) for each artery and bronchus. The image processing methods described in this study (Section III) can measure four to six diameters (Fig. 2) based on the size of the objects. The start and endpoints (x_1, y_1) and (x_2, y_2) of the (4 or 6) diameters are found by computing the pixel distance (Euclidean) between every combination of border pixels (Fig. 2) in an object (airway, artery) boundary and finding the pairs that range from maximum to minimum lengths. Section III explains the algorithm proposed in this research to find and compute the diameters.

Currently, clinicians depend on personal observations by using electronic calipers to measure the BARs of the lung C.T. images to diagnose bronchiectasis [15]. In research, multiple measurements are recorded, and the mean values are used for the BARs. These approaches are very time-consuming, especially when evaluating the entire airway structure. Currently, there needs to be more published literature on the automated detection of B.A. pairs and their BARs in HRCT scans of adults. There is even less for children. Prasad. et al. [21] proposed a three-stage process involving detecting potential bronchovascular pairs, detecting discrete pairs, and identifying abnormal pairs with severity levels. They demonstrated that their automated scoring system was comparable to an experienced radiologist's (*kappa* > 0.5).

Similarly, Odry et al. [22] demonstrated that automatically selected arterial regions agree with those chosen by human readers in 75.3% of the cases, compared to a 65.6% agreement between human readers. They also found that the computer-reader variability in measuring the lumen diameters was slightly lower (7%) than that of the human readers. They concluded that this variability is acceptable, and their automated system can provide an accuracy comparable to that of human readers. The experimental results of Naseri et al. [23] also demonstrated that semi-automated methods can measure the airway and adjacent vessel dimensions better than most existing methods. Techniques such as thresholding [24], [25], full-width-half maximum (FWHM) [26], [27], phase congruency [28], and model-based methods [29] are used to measure the diameters of inner airways and arteries, showing promising results.

To detect the B.A. pairs from the HRCT scans, one of the primary steps in our proposed method is to label the connected components of different objects. Labelling of connected components in a binary image is one of the most fundamental operations in image analysis, image understanding, pattern recognition, and computer vision [18]. It is handy in real-time applications such as automated surveillance and target tracking [30]. Several CCL algorithms have been proposed over the years [18] to improve the efficiency of labelling for real-time applications. Our optimized connected

components labelling algorithm allows us to identify the edges of various objects in a binary image of an HRCT scan created using pre-defined conditions for airway and artery regions. These edges are used to draw bounding boxes around the objects (inner airway, outer artery) and extract ROIs (discrete B.A. pairs) to measure their diameters and the B.A. ratios. The extracted ROIs can also allow us to assess many radiographic features of bronchiectasis, but this research mainly focuses on increased B.A. ratio, which is a primary pediatric radiographic sign seen in HRCT scans.

The methods proposed in this research are based on the 2D plane, which presents various anatomical structures of the bronchial tree in a flat way, which does not represent the curvatures and intricate details of the tree. Moving from 2D to 3D imaging methods may enhance the accuracy and reliability of evaluating the entire bronchial tree. This can help to monitor and assess changes in the bronchial structures effectively. Our proposed methods are designed to expand them in the future to generate 3D reconstructed models of bronchial structures. Various advanced image segmentation and recognition studies in the medical field have shown promising results using 3D-based methods. These studies described improvements compared to the 2D level, such as incorporating the spatial information to account for depth and perspective [37], [38], [39], transforming 2D segmentation methods into a volumetric approach (combining multiple planes (axial, coronal, sagittal)) [40], [41], [42], capturing long-range dependencies for precise segmentation using graph-based models [43], and the use of neural networks to capture the 3D structures using the relationships across multiple 2D slices [44], [45]. Our primary goal with our proposed 2D methods is to expand them in the future, using knowledge of clinical and radiographic features related to bronchiectasis. Developing novel 3D reconstruction methods can help us relate variations in a lobe or the tree to clinical aspects based on input from radiologists and clinical experts.

B. NOVELTY OF THE PROPOSED METHODS IN BRONCHIECTASIS STUDIES

The approach introduced in this study is distinct from conventional studies in bronchiectasis diagnosis. The emphasis of most studies is primarily on adult cohorts, whereas this study focuses on pediatric patients, highlighting their unique anatomical differences and variations in airway structures. Other contributions compared to existing studies related to bronchiectasis diagnosis are:

- Novel Image-Processing Methods: We introduce an optimized connected component labelling (CCL) algorithm for bronchiectasis diagnosis. The algorithm is tailored to the objects (airway, artery, veins, trachea, etc.) it is detecting. This allows us to differentiate variations between each object's lobes (upper, middle, lower). For example, it is evident that the size of bronchi and arteries gets smaller as we branch out further into the bronchial. Using various size conditions, anatomical differences can be detected.
- Novel Implementation for Diameter Measurement: This method uses a streamlined process to calculate diameters. Our method can reduce inter-rater variability by calculating the average of multiple diameters (4 or 6) for each object within the regions of interest (ROIs). Most existing studies in the 2D plane have either used the average of the minimum and maximum diameters or minor and major axis lengths. The proposed method allows us to store all the coordinates that are part of an object's perimeter boundary. This can facilitate more comprehensive analysis and measurements of broncho-arterial abnormalities.
- Validation Against Diverse HRCT Scans: The proposed methods are validated against various diverse HRCT scans from various categories (Infants, Early Childhood, Middle Childhood) and thickness/lengths (0.67/1/2/3/5 mm). This indicates that the proposed methods can be used across different scan types and patient conditions, something that has not been extensively explored in existing studies.
- Utilization of Full-Length CT Scans: The proposed methods utilize full-length C.T. scans instead of single images. This allows for a more comprehensive evaluation of broncho-arterial abnormalities.
- 3D Volume Creation from Extracted Coordinates: The proposed 2D methods can extract the inner airway and artery regions from an ROI (B.A. pair) and store them as coordinates. This can allow us to expand the current methods in the future to stack a series of frames of the C.T. scans and create 3D volumes of segments and sub-segments in the bronchial tree of a patient. The current methods are proposed with the intention of expanding them towards 3D imaging.

In essence, this study distinguishes itself from the existing studies through its emphasis on pediatric patients and novel image-processing methods/approaches tailored for the detection and measurements of the objects in the B.A. pairs. The utilization of full-length C.T. scans and the potential for 3D volume creation from extracted coordinates in the future can offer a more comprehensive approach and analysis for diagnosing bronchiectasis.

II. MATERIAL AND METHODS

A. DATA DESCRIPTION

The data is from a large pediatric prospective study (HREC 07/63) conducted at Royal Darwin Hospital, Northern Territory, Australia. Each subject in the data showcased some clinical symptoms related to bronchiectasis. The Human Research Ethics Committee (HREC), Menzies School of Health Research has provided the ethical clearance to use the de-identified HRCT scans from Royal Darwin Hospital, Darwin, Australia (Approval Code: HREC-07/63 and Date: Apr 22, 2022).

HRCT imaging of the lungs is a well-established technology for diagnosing and monitoring airway diseases. Optimal acquisition and interpretation of HRCT images requires both knowledge of anatomy and pathophysiology [31], and familiarity with the underlying physics and engineering principles of C.T. Although many of the operations of a C.T. scanner are automated, many technical parameters remain operator-dependent [31]. The parameters used significantly affect the diagnostic value of an HRCT examination. As shown in Table 1, researchers must provide the technical parameters used to collect their data.

1) DATA INCLUSION AND EXCLUSION IN CT SCAN COLLECTION

The original collection comprises of C.T. scans obtained from various scanners over time, each with varying resolutions and angles. For this study, we selected the C.T. scans (Subjects) collected with a specific scanner (Philips Ingenuity Core 64). For each subject, a minimum of six C.T. scans were used, with thicknesses varying from 0.67 to 9 mm. However, not all the subjects have an identical number of C.T. scans. Therefore, initially, we selected only 0.67 mm C.T. scans (as they hold more information than other scans), and after that, we used a random selection process to select 1/2/3/5mm C.T. scans. Based on the criteria described below, we categorized the C.T. scans according to age groups.

In children, airway size can be influenced by various factors, including age, height, weight, body composition, and underlying health conditions. The anatomical differences and variations in airway structures between infants, early Childhood, and middle Childhood can impact how images are processed and analyzed. Manual inspection of the available C.T. scans reveals that younger children generally have smaller airways than older children and adolescents. This is unsurprising in the context of children's development/growth of body size and anatomy over time.

Therefore, we've created three categories of full-length HRCT scans for different age groups: Infants (under two years), Early Childhood (2)-6 years), and Middle Childhood (6-12 years). Working on these categories allowed us to check the differences between the required image processing parameters (for detecting and measuring B.A. pairs) by validating the methods against a large number of full-length scans and proving the significance of the proposed methods for real-life scenarios.

Each category consists of 10 - 25 full-length axial plane HRCT scans that are reconstructed with slice thickness and intervals of 0.67 mm, 1 mm/2 mm/3 mm, and 5 mm. These HRCT scans belong to various subjects who showed clinical symptoms of bronchiectasis. All the HRCT scans are divided into two sets, one for testing and validating the proposed methods and the other to prove its statistical significance (Table. 1). Set 1 consists of 15 full-length HRCT scans reconstructed with a slice thickness of 0.67mm. Set 2 consists of 41 full-length HRCT scans of lengths 1/2/3/5 mm. They were all imaged using a high-resolution 64-slice Multi-Detector CT (MDCT) capable of acquiring near-isotropic data throughout the thorax in a single breath-hold. This permits the acquisition of volumetric single-breath-hold datasets, allowing spaced, contiguous, and overlapping HRCT images to be reconstructed. With MDCT, the volumetric data enables multiplanar (axial, coronal, sagittal) thin-section HRCT reconstruction (MPR). Each subject in this study had ∼9 types of reconstructed images from different planes. Each patient was imaged without any intravenous contrast enhancement, and the images were created using a standard reconstruction kernel and stored in DICOM format. Table. 1 provides the technical parameters and number of slices available for each patient at different intervals/thicknesses.

TABLE 1. Technical parameters: The categories and their associated scans from different reconstruction lengths.

Scanner: Philips Ingenuity Core 64 Technical Parameters Acquisition Mode: Spiral (or Helical); Single Collimation Width: 0.625 mm Total Collimation Width: 64 x 0.625 = 40 mm Spiral Pitch Factor: 1.725; Kilovoltage Peak: 80 kVp; Gantry Tilt: 0; DFOV (Average): 170 mm; Estimated Dose Saving (Average): -10			
Category	0.67 mm	1/2/3 mm	5mm
Infant (< 2 years)	5	10	3
Early Childhood (2 – 6 years)	7	14	5
Middle Childhood (6 – 12 years)	2	6	3
Total Scans	**14**	**30**	**11**
Set	**Testing**	**Statistical Significance**	

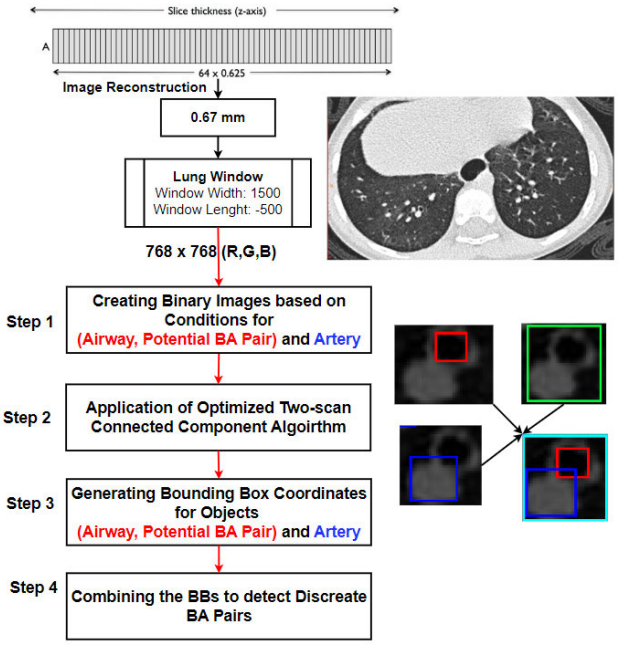

FIGURE 3. Steps to detect discrete B.A. pairs.

B. LOCATING AIRWAYS, ARTERIES/VEINS, POTENTIAL B.A. PAIRS, AND DETECTING DISCRETE B.A. PAIRS

Locating discrete B.A. pairs involves constructing bounding boxes (B.B.) (Fig. 3) around the relevant objects: inner airways (red), arteries (blue), and potential B.A. pairs (green). Constructing the B.B.s for each object requires similar steps but with different size conditions. The generated B.B. coordinates of the objects are drawn in their respective frames (Fig. 3). This allows us to identify locations of discrete B.A. pairs, with red and blue B.B.s inside a green B.B. Fig. 3 illustrates the step-by-step process proposed in this research to detect the discrete B.A. pairs.

The frames for the HRCT scans were created using the C.T. lung window (W: 1500, L: -500). The frames are 768 × 768 and have three channels (R, G, B). The steps shown in Fig. 3 are applied to these frames to get the bounding box coordinates for all the objects and detect the discrete B.A. pairs. The following steps and the pseudocodes explain the process of locating the objects and detecting the discrete B.A. pairs.

1) STEP 1: CREATING BINARY IMAGES BASED ON CONDITIONS

The algorithm for step 1 is used for pre-processing the slices so that the connected components algorithm in step 2 can generate the B.B.s. We applied two conditions to replace the pixel values in a grayscale DICOM image with two RGB values. The condition rgb[0] <= 20 (R-value) creates the binary images that are used to detect the inner airway and potential B.A. pair B.B.s. It replaces the pixel values that are below 20 with (0,0,0) and the rest with (80,80,80) or another single RGB value (>= 80). Similarly, the condition for arteries/veins, rgb[0] <= 45, is used to replace all the pixel values that are below 45 with (0, 0, 0) and the rest with (80, 80, 80) or another single RGB value (>= 80) in the lung window images. This process is illustrated in Pseudocode. 1.

Pseudocode 1

Step 1: Creating Binary Images

```
pixel1 = [ ]
pixel2 = [ ]
coordinates = [ ]
for a in range(0, width):
   for b in range(0, height):
      rgb = px[a, b]
      coordinates.append([a,b])
      if rgb[0] <= 20:    //Airway, Potential Pair
         pixel1.append((0,0,0))
      else:
         pixel1.append((80,80,80))
      if rgb[0] <= 45:    //Artery
         pixel2.append((0,0,0))
      else:
         pixel2.append((80,80,80))
```

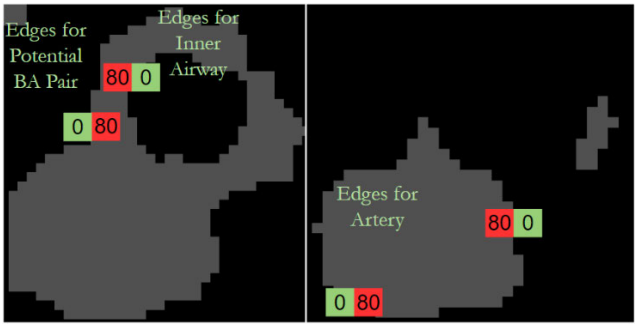

FIGURE 4. Types of edges for inner airway, potential B.A. Pair, Artery.

2) STEP 2: APPLICATION OF OPTIMIZED TWO-SCAN CONNECTED COMPONENTS LABELLING (OCL) ALGORITHM

In graph theory, connected components are subgraphs of a connected graph, connected to no other node in the super graph, and have paths only between two nodes. The same concept can be applied to the connected components in an image because images are a 'grid of pixels (nodes)' that are connected by edges (Grid Graph [19]). The algorithm looks for pixels with the same value connected through 'four-pixel' connectivity along the edges. Here, an edge is defined as a pixel whose grey level differs from an adjacent pixel's (Fig. 4).

The binary image generated for airways and potential B.A. pairs has two types of edges: 80 –> 0 and 0 –> 80 (Fig. 4). Using the matching pixel (0,0,0) allows the algorithm to find a set of coordinates (connected components) along the inner airway boundaries in the binary lung window images. Similarly, the matching pixel (80,80,80) allows the algorithm to get boundary coordinates for potential B.A. pairs. To generate the connected components for the arteries, the algorithm uses the same binary lung window image to look for edges 0 –> 80, using the matching pixel (80,80,80); and finds a set of coordinates for the artery boundary.

These sets of coordinates are used as inputs for the first scan (Pseudocode 2) of the OCL algorithm to generate all pairs of neighboring pixels. The neighboring pixels are generated similarly to most conventional labelling algorithms [18]. The first scan assigns a provisional label to each foreground pixel. For an N x N binary image, we use *p(x, y)* to denote the image's pixel value at coordinate (x, y). For the pixel *p(x, y),* the pixels *p(x-1, y-1), p(x, y-1), p(x+1, y-1), p(x-1, y)* are the four connected neighbors, as illustrated in Pseudocode 2 (first scan). The coordinates generated for the neighboring pixels are inputs for the second scan (Pseudocode 2) of the OCL algorithm, which generates connected components as a set of nodes (or coordinates).

After the first scan generates all the neighboring pairs for the matching pixels, the second scan finds a representative label for each group of equivalent neighboring pairs and relabels all the foreground pixels in the first scan with a usual label. This allows us to detect the connected components (edge coordinates) for the inner airways, potential B.A. pairs, and arteries.

Pseudocode 2 First Scan: Generate All Pairs of Neighboring Pixels

```
Function neighbors(coordinates)
  coordinates = set(coordinates)
  for x, y in coordinates:
    if (x - 1, y - 1) in coordinates:
      yield (x, y), (x - 1, y - 1)
    if (x, y - 1) in coordinates:
      yield (x, y), (x, y - 1)
    if (x + 1, y - 1) in coordinates:
      yield (x, y), (x + 1, y - 1)
    if (x - 1, y) in coordinates:
      yield (x, y), (x - 1, y)
    yield (x, y), (x, y)
```

Pseudocode 2 Second Scan: Generate Connected Components as Set of Nodes

```
Function connected_components(edges):
  neighbors = defaultdict(set)
  for a, b in edges:
      neighbors[a].add(b)
      neighbors[b].add(a)
  seen = set()
  Function component(node, neighbors=neighbors,
          seen=seen, see=seen.add):
    unseen = set([node])
    next_unseen = unseen.pop
    While unseen:
      node = next_unseen()
      see(node)
      unseen | = neighbors[node] - seen
      yield node
  Return (set(component(node)) for node in neighbors if node not in seen) //(coordinates)
```

3) STEP 3: GENERATING BOUNDING BOX COORDINATES FOR OBJECTS (INNER AIRWAY, POTENTIAL BA PAIR, ARTERY)

To generate the bounding box coordinates for each object, the minimum and maximum values ((min(xs), min (ys), max(xs), max(ys)) are computed for each set of edge coordinates generated in the previous step, this is illustrated in Pseudocode 4 below.

Using the formula for the rectangular area (area = length ∗ width), the area for the bounding boxes is computed and filtered based on five conditions (Fig. 5):

- Condition 1 (50 <= area <= 500) is used to draw the bounding boxes for the inner regions of medium-to-small airways of potential B.A. pairs, outlined in red (255,0,0) in Fig. 5.
- Condition 2 (20 <= area < 50) is used for the rest of the inner airway regions.
- Condition 3 (500 < area <= 1000) is used to find the bounding boxes for potential B.A. pairs, outlined in green (0,255,0) in Fig. 5.

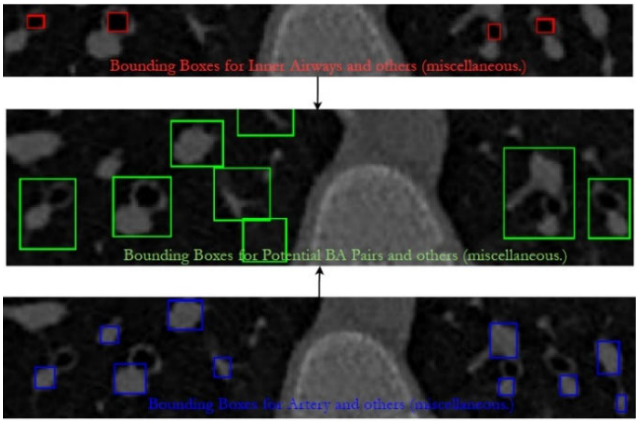

FIGURE 5. Bounding boxes for various objects detected in a portion of a C.T. scan using multiple conditions.

Pseudocode 3

```
Function boundingbox(coordinates):
  xs, ys = zip(∗coordinates)
  co = [(min(xs), min(ys), max(xs), max(ys)]
  //example [(221,470, 231, 477)]
  realco = [ ]
  for cords in co:
    a = cords[0]; b = cords[1]; c = cords[2];
    d = cords[3];
    length = c - a
    breadth = d - b
    area = length ∗ breadth //area of rectangle
    if 50 <= area <= 500:
      realco.append((a,b,c,d))
    for rect in realco:
    draw.rectangle(rect, outline=(0, 255, 0))
```

- Condition 4 (50 <= area <= 500) uses the same filter as Condition 1, but it is used to draw the bounding boxes for small to medium arteries/veins, outlined in blue (0,0,255) in Fig. 5.
- Condition 5 (500 < area) is used for larger or remaining arteries/veins.

4) STEP 4: COMBINING THE BOUNDING BOXES TO DETECT DISCRETE BA PAIRS

All the bounding boxes generated are plotted on their respective slices/frames (i.e., red /and blue boxes inside green boxes), as shown in Fig. 6. This allows us to write a program that can easily identify the regions that contain boxes of all three colors together (i.e., red and blue inside green). Once such regions are identified, they are outlined by replacing the green boxes with cyan boxes (Fig. 6). These cyan boxes indicate the presence of discrete B.A. pairs. The bounding box coordinates for all cyan boxes are saved in a CSV file for further processing.

The image processing steps allowed us to locate most large-to-small airways and arteries/veins and detect most of

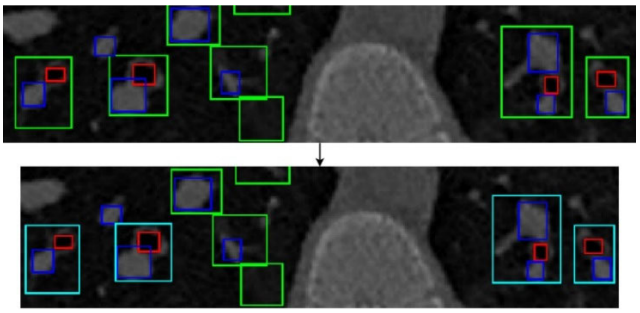

FIGURE 6. Combining all the B.B.s and converting the green boxes to cyan (0, 255, 255).

the discrete B.A. pairs in the axial plane images, reconstructed with thickness and intervals of 0.67 mm.

C. BAR

One of the primary steps to measure the BAR is to get the perimeter coordinates for the inner airway and outer artery objects and calculate the Euclidean distance between each combination. Using the distances and their coordinate combinations, our method can select four or six combinations that pass through or near the center of an object and calculate their average (i.e., the mean diameter). This process involves five steps:

- Extracting ROIs, the patches inside the Cyan bounding boxes.
- Processing/enhancing these patches.
- Detecting 'matching sequences' of pixel values in each row of the patch and constructing the coordinates for the regions of the objects.
- Obtain the coordinates for the perimeter of the objects and calculate the Euclidean distances.
- Selecting four or six diameters for the objects, taking the average, and calculating the BARs.

1) STEP 2: PROCESSING/ENHANCING ROI PATCHES

The algorithm for Step 2 is used for pre-processing the ROIs so that the object's region can be detected easily. The algorithm uses two conditions to replace the pixel values in a grayscaled ROI patch. The condition rbg[0] <= 20 (R-value) is used for the airway region to remove the noise (replace with (0,0,0)) and improve the soft-tissue intensity (80,80,80) in the ROIs (Fig. 7). Similarly, the conditions rbg[0] <= 20, 20 < rgb[0] <= 45, and 45 < rgb[0] <= 100, are used for the artery region to replace the pixel values with (0,0,0), (255,0,0), and (80,80,80) respectively (Fig. 7).

2) STEP 3: MATCHING SEQUENCES AND CONSTRUCTING COORDINATES FOR THE INNER AIRWAY AND OUTER ARTERY REGIONS

This step allows us to check the 'Matched Sequences' in the pixel values of each row of a Processed ROI and construct the coordinates for the Inner Airway and Outer Artery regions. Once the ROIs are processed, we use the Pseudocode for

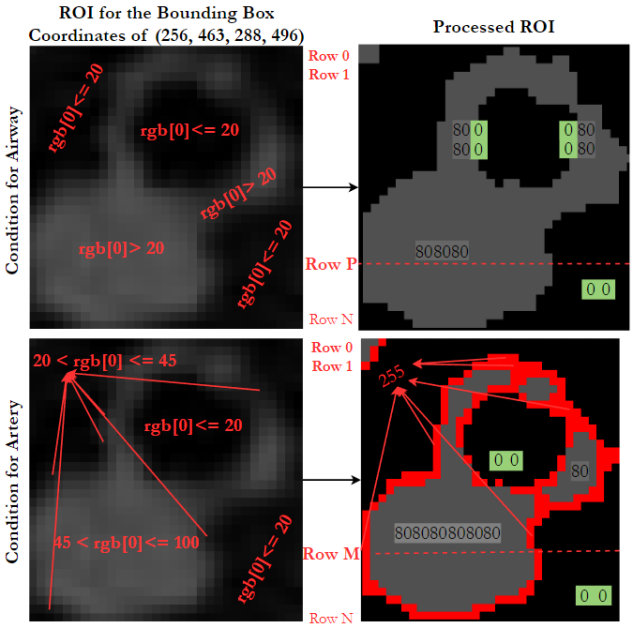

FIGURE 7. Step 2 - conditions for processing ROIs.

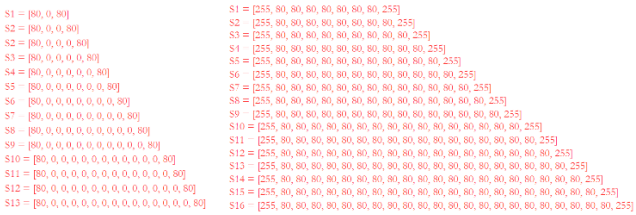

FIGURE 8. Matching sequences (inner airway & outer artery).

step 3 to get the list of pixel values (rgb[0] (R-Value)) in each row (Fig. 7) of the ROI. For example, in **Row M** in Fig. 8 (red line), the list of pixels in the processed artery ROI is [0, 255, 80, 80, 80, 80, 80, 80, 80, ..., 255, 0, 0, ..., 0]. Similarly, the list of pixels in **Row P** of the processed Airway ROI looks like [0, 0, ..., 80, 80, 80, 80, ..., 0, 0, 0]. Most of the rows in the processed ROI follow the same pattern. In the pixel value lists for the airway and artery, the algorithm will look for matching sequences (Fig. 8) and return their index positions in the list as a range (output example Pseudocode. 4.1).

The row.items() in Pseudocode. 4.1 represents a dictionary with rows and their list of pixel values (R values). All the sequences in Fig. 8 are checked in each row of the processed airway ROI (Fig. 7), and the index numbers (column numbers) for the matches are combined, as shown in the output example of Pseudocode. 4.1. Here, the index is the column number in a row where a pixel match is found.

For 'row463' in the output example (Pseudocode. 4.1), the values (257, 273) represent the column numbers (or index positions) between which a matching sequence (Fig. 8) is found. Using the row number and the column range, the algorithm (Pseudocode. 4.2) can get all the coordinates that

Pseudocode 4.1

```
m = {}
for a, b in row.items():
   g1 = [(i, i+len(S1)) for i in range(len(b)) if
b[i:i+len(S1)] == S1]
   g2 = [(i, i+len(S2)) for i in range(len(b)) if
b[i:i+len(ff)] == S2]
   g3 = [(i, i+len(S3)) for i in range(len(b)) if
b[i:i+len(gg)] == S3]
   g4 = [(i, i+len(S4)) for i in range(len(b)) if
b[i:i+len(hh)] == S4]
   :
   gn = [(i, i+len(Sn)) for i in range(len(b)) if
b[i:i+len(Sn)] == Sn]
   m[a] = g1 + g2 + g3 + g4 +.. +.. + gn
```

Output (Example)

```
{'row463': [(257, 273)],
'row464': [(256, 271), (506, 524)],
'row465': [(254, 270), (506, 524)],
'row466': [(506, 524)]}
```

are part of the inner airway and the outer artery regions, as shown in the output example of Pseudocode 4.2.

Pseudocode 4.2

```
row = 0
AirwayCos = []
for x, z in m. items()
for y in z:
    value = y[0]
   value 1 = y[1] − 1
   for i in range (1, value 1 -
value):
    value 2 = value +i
   AirwayCos.append
([value 2, p])
p = p + 1
```

```
row = 0
ArteryCos = []
for x, z in m. items ():
    for y in z:
    value = y[0]
value 2 = y[1]
   for i in range (0,
value 2 - value):
    value 2 = value +i
    ArteryCos.append
([value 2, p])
p=p + 1
```

Output (Example) for 'row463':[[258, 463], [259, 463], [260, 463], [261, 463], [262, 463], ... [272, 463]]

For most of the processed ROIs (airway and artery), the obtained coordinates cover their respective object regions accurately (Fig. 9). In some cases, there can be a few coordinates missing, similar to No. 2 in the artery region (Fig. 9)), which can be dilated later using a (2, 2) kernel.

3) STEP 4: PERIMETER COORDINATES AND THEIR EUCLIDEAN DISTANCES

After filling the constructed coordinates with different pixel values, we apply conventional methods, such as detecting contours or blobs. Step 4 allows us to get the coordinates of the object contours (inner airway, artery) from the filled regions (Fig. 9). To draw a perimeter around the object, the algorithm uses the drawContours() function of OpenCV (cv2.drawContours(ROI, contours[i], contourIdx = −1, color = (r, g, b), thickness = 1) to overlay the contours on the ROI. Using a thickness of 1 allows the algorithm to overlay the contour boundary (or perimeter), as shown in Fig. 10.

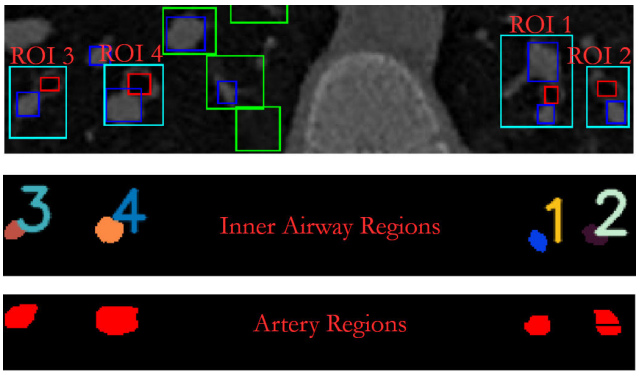

FIGURE 9. Plotting the constructed coordinates for inner airway and outer artery.

Using the perimeter coordinates, Pseudocode 5 calculates the Euclidean distance between each combination of boundary pixels of an object. For example, to get the perimeter coordinates for the 'orange-colored airway' in Fig. 10, we need to get all the coordinates with blue (3, 117, 186) pixels and compute the Euclidean distances between each combination.

Pseudocode

```
co = ⌈⌉
for a in range (0, w):
for b in range (0,  h):
 rgb = px[a, b]
 if rgb = (3, 117, 186):
  co.append ((a, b))
// Coordinates
```

```
dis = ⌈⌉
for i in range(len(co)):
 for i in range (i + 1, len(co)) :
 distance =math.dist(co[i],
          co[j])
 dis.append((co[i],
    co[i], distance))
dis.sort(key=lambda x:
(-float(x[2]),
x[1], x[0]), reverse=True)
```

4) STEP 5: SELECTING FOUR OR SIX DIAMETERS FOR THE INNER AIRWAY AND OUTER ARTERY REGION AND THEIR BAR

Once all the distances for the combinations are calculated, they are appended to a list in this format: ((269, 476), (282, 471), 13.93). Here, the Euclidean distance is in pixels (px). After appending to a list, the numbers (float) in the list are sorted using a lambda function so that the algorithm can access the combination that has 'maximum Euclidean distance' (MED) (dis[-1]). The MED is also the measure of an object's length. Drawing a line using that combination will always produce a 'major axis' (M.A.) (the longest line that can fit an object), which passes through (or near) the object's center. The algorithm in step 5 uses the major axis coordinates of an object to find the rest of the diameters (four or six). The number of diameters is dependent on the size of the objects. If the major axis length is >20px, six diameters are measured for the objects. Similarly, if the length is < 20px,

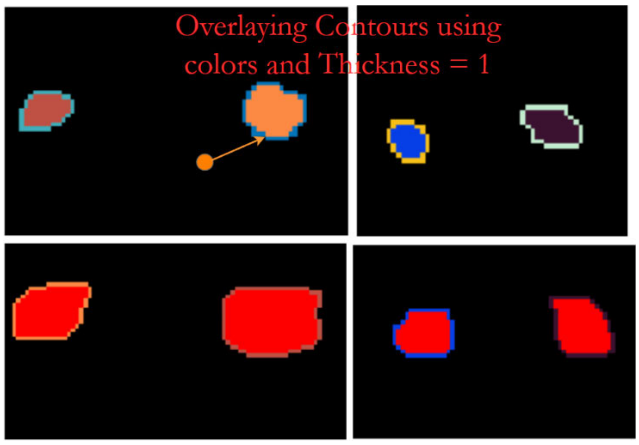

FIGURE 10. Contour boundary (perimeter) of the objects in different colors.

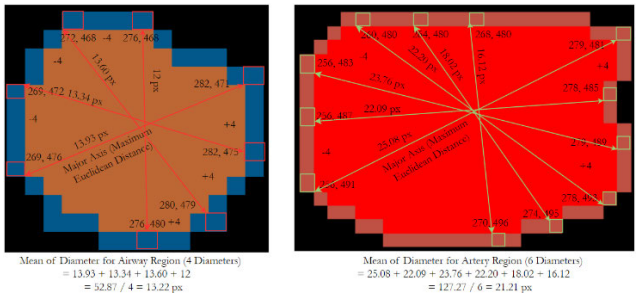

FIGURE 11. Diameter endpoints for inner airway (4) and outer artery (6).

four diameters are measured. The algorithm works by moving the coordinates of the major axis from both ends. One end of the axis will move by -4 and the other by +4, based on the size. This produces two new coordinates as endpoints that pass through (or near) the center of the object (Fig. 11). This process is repeated till four or six diameters (endpoints) are found for an object (major axis + others). Once found, the algorithm calculates the Euclidean distance between the endpoints and averages them to produce diameters for the inner airways and outer arteries (Fig. 11).

Using the diameters for the inner airway and artery region, we calculate the BAR ratio (13.22 px:21.21 px) to check whether the B.A. pair is abnormal (signet-ring appearance and/or increased BAR (>0.8)) or not. The BAR (13.22/21.21) for the pair shown in Fig. 11 is 0.62, less than 0.8, indicating that this B.A. pair is normal.

III. RESULTS AND DISCUSSION

A. TESTING THE PROPOSED DETECTION METHOD WITH SET 1

Set 1 consists of 15 HRCT scans that belong to various age groups: Infancy (5), early Childhood (7), and middle Childhood (3). We applied our proposed detection methods on these scans to locate the objects (airway, artery/vein, potential B.A. pair). Each HRCT scan consists of 400 – 600 frames of size 768 × 768. Table. 2 provides the number of frames

TABLE 2. Total number of located objects for each condition F: Number of frames, C1: medium-to-small airways (50 <= area <= 500); C2: Smaller Airways (20 <= area < 50); C3: Potential BA pairs (500 < area <= 1000); C4: medium-to-small artery/vein (50 <= area <= 500); TDBA: Total discrete BA pairs.

Category		F	C1	C2	C3	C4	TDBA
Infancy (< 2 y)	1	420	582	616	132	1034	32
	2	402	762	834	0	462	0
	3	465	546	915	10	694	5
	4	465	562	834	125	962	35
	5	412	746	819	110	669	28
Early Childhood (2 – 6 y)	1	537	948	540	328	3505	52
	2	465	752	335	410	4364	39
	3	420	762	543	365	2468	33
	4	535	648	792	262	3224	46
	5	535	862	934	190	1462	33
	6	551	646	815	210	1694	45
	7	482	585	678	135	1247	29
Middle Childhood (6 – 12 y)	1	689	1071	226	184	4679	54
	2	1378	1876	458	289	6342	79

available in each scan (0.67 mm) and the number of objects located using each bounding box area condition. Using different conditions (Table. 2) allowed us to differentiate between airways and artery/vein structures in the HRCT scans and assess the differences among various age groups. Most differences can be noticed in the number of objects located using each condition. This could be because their anatomy is still developing, and their airways need to grow and mature over time. Table. 2 provides a comparison between various categories.

In the Infancy (< 2 years) category, the number of smaller airways (20 <= area <= 50) detected using our methods is more when compared with other categories; this is despite having a smaller number of frames. Most airways are below 50 (area) for infancy subjects and above 50 for most early and middle childhood subjects. A significant difference is noticed in the C3 and C4 conditions, where the proposed methods have detected fewer potential disjoint B.A. pairs for the infancy subjects and healthy numbers for other categories. Manual inspection of the HRCT scans also reveals the same. In some cases, the number of potential B.A. pairs (C3) detected can be fewer. This can signify that the subject has some disease/abnormality related to the airways or lungs, as shown in Fig. 12. Comparing the results of various categories of conditions C1, C3, and C4 also indicates that the number of detected objects increased with age.

1) PROVING STATISTICAL SIGNIFICANCE USING SET 2

Set 2 consists of 41 HRCT scans of lengths 1/2/3 and 5mm. The number of frames drastically decreases as the length/thickness increases from 0.67 mm (Table. 3). Proving the statistical significance of a method for object detection in images typically involves rigorous experimentation and statistical analysis. It is important to remember that proving statistical significance doesn't always guarantee the real-world effectiveness of the proposed method. To enhance the robustness and reliability of our statistical analysis,

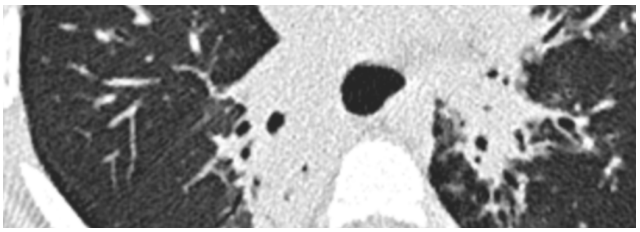

FIGURE 12. A frame from an HRCT Scan from the infancy category showing signs of a disease.

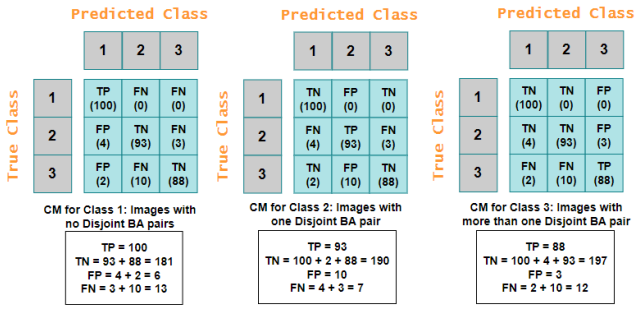

FIGURE 13. Confusion matrixes for individual classes.

we have created multiple sets (X1, X2, and X3) using the 41 HRCT scans from Set 2. Each set (X) consists of HRCT scans that belong to a specific age category. In these sets (X), all the frames in their respective scans are combined and divided into three classes of images: 1) Images with No B.A. Pairs, 2) Images with one Disjointed B.A. Pair, and 3) Images with more than one Disjointed B.A. Pair. After manually inspecting the HRCT scans and drawing the bounding boxes for the Disjointed B.A. pairs, the frames are divided into their respective classes. We have used evaluation metrics such as Precision (P) and Recall (R) to provide insights into how well the proposed method can detect the objects in the images. To calculate these metrics for each class, we should initially measure the true positive (T.P.), true negative (T.N.), false positive (F.P.), and false negative (F.N.) values for each class separately by following the confusion matrixes shown in Fig. 13. Fig. 13 also provides the values for all the classes in set X1 separately.

To calculate the evaluation metrics for each class, we should first generate the values for Precision and Recall using the definitions provided below:

$$Precision\ (P) = \frac{TP}{TP + FP} \tag{1}$$

$$Recall\ (R) = \frac{TP}{TP + FN} \tag{2}$$

Using the confusion matrixes in Fig. 13, we repeated the same approach to get the T.P., TN, F.P., and F.N. values for the classes in sets X2 and X3, as shown in Table. 3. We have used Macro Precision and Macro Recall scores to treat all the classes in a set (X) equally and evaluate the algorithm's performance across all the classes in one value.

TABLE 3. True positive, true negative, false positive, false negative, precision, and recall values of different classes in each set.

Set		Images	T.P.	T.N.	F. P.	F.N.	P (%)	R (%)
X1 (I)	1	100	100	181	6	13	94.3	88.5
	2	100	93	190	10	7	90.3	93
	3	100	88	197	3	12	96.7	88
X2 (E.C.)	1	100	100	184	5	7	95.2	93.5
	2	100	96	195	5	4	95	96
	3	100	92	198	2	8	97.9	92
X3 (MC)	1	100	100	187	5	8	95.2	92.6
	2	100	91	198	2	9	97.8	91
	3	100	96	194	6	4	94.1	96

The Macro scores are computed by averaging all the precision and recall values in a set. For example, the Macro Precision and Recall scores for set X1 are obtained by averaging $(94.3 + 90.3 + 96.7)/3$ and $(88.5 + 93 + 88)/3$, which is 93.8% and 89.8 %. Similarly, we computed the Macro scores for sets X2 and X3, yielding 96.03 % and 95.7% for precision and 93.8% and 93.2% for Recall.

B. VALIDATING THE BA RATIOS WITH MANUAL READINGS

Using the proposed 2D measurement method, the size of various anatomical structures can be quickly and easily determined, making it useful for routine clinical practice. However, it assumes that the structure being measured is approximately circular on the 2D plane, which may only sometimes be the case. Also, the root problem with 2D imaging/measurements is that it fails to consider body curvature, especially for surfaces such as the chest and abdomen, leading to inaccurate measurements. Therefore, to validate the proposed methods, we have compared our automated results with manual measurements from ImageJ software (Table. 4). The manual measurements are taken from the unprocessed original scans and done twice (M1 and M2) to consider potential 'human error' during measurements. In geometry, an ellipse is a closed curve that looks like a stretched-out circle. It has two main axes: the major axis and the minor axis. The major axis is the longest diameter of the ellipse that travels through the center from one end to the other. The minor axis is the shortest diameter of the ellipse perpendicular to the major axis. We averaged the major and minor axes' lengths to get the manual measurements/diameters for the airway and artery, as shown in Table. 4 The proposed method requires the object's contour (ROI coordinates in Table. 4) as input to perform the measurements. Therefore, we selected 12 disjoint B.A. pairs from the HRCT scans of six subjects (2 each).

The results in Table. 4 shows that the diameters from our proposed methods are in agreement with the manual measurements, assuring that our methods can provide reliable B.A. ratios for the detected disjoint B.A. pairs.

IV. LIMITATIONS

While this study provides valuable insights into detecting and measuring broncho-arterial pairs in pediatric chest C.T. scans, several limitations should be acknowledged.

TABLE 4. Automated vs. manual measurements inner airway and artery diameters (in pixels) from 12 B.A. Pairs.

Fr.	B.A. Pair ROI Cord.	Inner Airway	Manual Measurements		Artery	Manual Measurements	
			M1	M2		M1	M2
P1 134	(260,366,296, 395)	9.74	(11.19 + 8.39) / 2 = 9.79	(11.30 + 8.55) / 2 = 9.92	15.23	(17.04 + 14.27) / 2 = 15.65	(18.16 + 13.07) / 2 = 15.61
			Avg. = 9.85			**15.63**	
238	(190,325,229, 356)	11.73	(15.17 + 8.23) / 2 = 11.70	(14.87 + 8.44) / 2 = 11.65	15.72	(16.64 + 13.80) / 2 = 15.22	(17.75 + 14) / 2 = 15.87
			11.67			**15.54**	
P2 296	(209,460,238, 489)	8.03	(9.57 + 7.19) / 2 = 8.38	(9.05 + 6.22) / 2 = 7.64	14.42	(16.23 + 12.77) / 2 = 14.5	(16.38 + 13.42) / 2 = 14.9
			8.01			**14.7**	
300	(205,464,235, 493)	9.14	(11.28 + 6.28) / 2 = 9.05	(9.28 + 7.23) / 2 = 8.52	14.32	(15.84 + 13.52) / 2 = 14.68	(17.33 + 10.85) / 2 = 14.09
			8.78			**14.38**	
P3 261	(159,300,178, 317)	5.68	(6.35 + 5.46) / 2 = 5.90	(6.80 + 4.27) / 2 = 5.54	12.47	(15.53 + 9.84) / 2 = 12.68	(14.67 + 10.17) / 2 = 12.42
			5.72			**12.55**	
262	(159,299,178, 318)	5.30	(6.13 + 4.13) / 2 = 5.13	(6.87 + 4.37) / 2 = 5.60	11.60	(14.17 + 9.01) / 2 = 11.59	(14.50 + 8.50) / 2 = 11.50
			5.36			**11.54**	
P4 259	(152,255,170, 271)	5.28	(5.78 + 4.96) / 2 = 5.37	(5.55 + 5.02) / 2 = 5.28	8.75	(8.88 + 8.84) / 2 = 8.86	(8.93 + 8.51) / 2 = 8.72
			5.32			**8.79**	
260	(152,256,169, 271)	6.18	(6.96 + 5.27) / 2 = 6.12	(7.12 + 4.77) / 2 = 5.94	8.51	(9.08 + 8.10) / 2 = 8.59	(8.85 + 8.33) / 2 = 8.59
			6.03			**8.59**	
P5 329	(154,335,170, 354)	4.82	(4.87 + 4.72) / 2 = 4.79	(5.10 + 4.40) / 2 = 4.75	9.21	(10.33 + 8.33) / 2 = 9.33	(10.13 + 8.50) / 2 = 9.31
			4.77			**9.62**	
330	(154,337,170, 354)	4.90	(5.32 + 4.30) / 2 = 4.81	(4.96 + 4.77) / 2 = 4.86	10.10	(11.79 + 8.60) / 2 = 10.19	(11.43 + 8.96) / 2 = 10.19
			4.83			**10.19**	
P6 311	(169,264,190, 288)	10.21	(11.40 + 8.90) / 2 = 10.15	(11.50 + 8.28) / 2 = 9.90	12.26	(13.50 + 11.17) / 2 = 12.33	(13.23 + 11.83) / 2 = 12.53
			10.02			**12.43**	
312	(170,263,191, 287)	10.58	(11.93 + 9.01) / 2 = 10.47	(12.09 + 8.67) / 2 = 10.38	12.78	(14 + 11.83) / 2 = 12.91	(13.67 + 13.01) / 2 =13.34
			10.42			**13.12**	

- Sample Size and Diversity: Initially, this research aimed to develop methods using C.T. scans with a thickness of 0.67 mm for each available patient. However, due to the limited availability, we decided to include C.T. scans of different dimensions (1/2/3/5 mm). Larger and more diverse cohorts of patients could provide a more comprehensive understanding of broncho-arterial pairs in other demographics.
- Variations Between Lobes: The asymmetrical nature of the lung lobes can lead to variations in the branching patterns of bronchi and arteries between different lobes. For instance, the left lung, comprised of two lobes, exhibits distinct branching patterns and dimensions compared to the right lung's three lobes. These asymmetries can pose a challenge in standardizing detection methods for broncho-arterial pairs across the entirety of the lungs. We believe that developing airway and artery 3D reconstruction methods in the future can help to improve standardization.
- Manual Annotations and Generalizability: While the study focuses on detection methods, the clinical significance or implications of identifying broncho-arterial

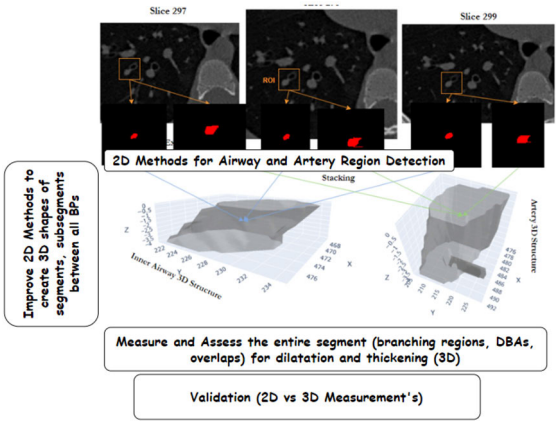

FIGURE 14. Stacking a series of frames with "ROI" to create 3D reconstructed models of the segments and subsegments between the branching points (B.P.s) in the bronchial tree and comparing the 3D measurement methods with 2D for validation.

pairs in children may not have been fully explored. This will be continued in the future work.

- Validation and Comparison with Gold Standards: There might be a lack of validation or comparison of the proposed methods with established gold standards or alternative techniques. Most of the existing research into this topic is based on adult cohorts and isolated scans, and a gold standard for children is still a topic of discussion. Comparison with state-of-the-art existing studies and developing 3D reconstruction methods may lead to better standardization.
- Constraints of 2D Representation: 2D imaging, like traditional C.T. scans, presents various anatomical structures of the bronchial tree in a flat two-dimensional plane), without capturing the curvature in the segments, sub-segments, and branching points of the bronchial tree. Assessing the extent of bronchial dilation solely in 2D can lead to inaccuracies, especially when measuring diameters or evaluating changes over time. Developing methods to generate reconstructed 3D models of the bronchial tree can help accurately capture its curvature and spatial relationships.

These limitations will be addressed in our future work. We aim to create a diagnostic tool for a specific lobe (lower lobe) by developing novel 3D reconstruction methods so that clinically relevant variations in that lobe (segments, subsegments, branching points) can be validated with the help of radiologists and clinical experts of this team.

V. CONCLUSION

In conclusion, the study introduces two novel methods for detecting and measuring broncho-arterial (B.A.) pairs in full-length HRCT scans of pediatric patients to assess increased BAR. To verify the practicability and reliability of these methods in children of different ages, the study conducted thorough validation by employing various HRCT scans (Infants, Early Childhood, and Middle Childhood) with thicknesses (0.67/1/2/3/5 mm). Metrics such as Precision and Recall are crucial in evaluating the detection method, particularly in medical imaging for object detection and localization. Averaging the precision and Recall scores obtained for each set yielded 95.17% ((93.8+96.03+95.7)/3) and 92.27% ((89.8+93.8+93.2)/3), showcasing promising results. Similarly, the findings from our validation study for the measurement method also showed encouraging results, as we observed minimal discrepancies when comparing them to manual measurements.

Consequently, these methods demonstrate significant potential to help enhance the domain of pediatric radiology. More specifically, these methods have the potential to help characterize additional notable radiographic features associated with bronchiectasis, such as bronchial wall thickening, bronchial tapering, and mucus plugging.

VI. FUTURE WORK

Our future work will explore 3D imaging methods, like volumetric C.T. scans or reconstructed 3D models. This may improve the accuracy, precision, and reliability of assessing and monitoring changes in the bronchial tree, potentially leading to more effective diagnosis and treatment plans.

In this research, we have proposed two methods for detecting and measuring the B.A. pairs instead of combining them into one form. This will allow us to expand our 2D-based detection method towards reconstructing specific segments and subsegments in the bronchial tree and comparing the results from 2D measurement methods with 3D techniques. Fig. 14 illustrates this.

REFERENCES

[1] A. B. Chang, K. Grimwood, J. Boyd, R. Fortescue, Z. Powell, and A. Kantar, "Management of children and adolescents with bronchiectasis: Summary of the ERS clinical practice guideline," *Breathe*, vol. 17, no. 3, Sep. 2021, Art. no. 210105, doi: 10.1183/20734735.0105-2021.

[2] A. B. Chang, A. Bush, and K. Grimwood, "Bronchiectasis in children: Diagnosis and treatment," *Lancet*, vol. 392, no. 10150, pp. 866–879, 2018, doi: 10.1016/S0140-6736(18)31554-X.

[3] G. B. McCallum and M. J. Binks, "The epidemiology of chronic suppurative lung disease and bronchiectasis in children and adolescents," *Frontiers Pediatrics*, vol. 5, p. 27, Feb. 2017, doi: 10.3389/fped.2017.00027.

[4] G. B. McCallum, V. M. Oguoma, L. A. Versteegh, C. A. Wilson, P. Bauert, B. Spain, and A. B. Chang, "Comparison of profiles of first nations and non-first nations children with bronchiectasis over two 5-Year periods in the northern territory, Australia," *Chest*, vol. 160, no. 4, pp. 1200–1210, Oct. 2021, doi: 10.1016/j.chest.2021.04.057.

[5] S. C. L. Hewer, "Is limited computed tomography the future for imaging the lungs of children with cystic fibrosis?" *Arch. Disease Childhood*, vol. 91, no. 5, pp. 377–378, May 2006, doi: 10.1136/adc.2005.086660.

[6] V. Goyal, K. Grimwood, J. Marchant, I. B. Masters, and A. B. Chang, "Pediatric bronchiectasis: No longer an orphan disease," *Pediatric Pulmonol.*, vol. 51, no. 5, pp. 450–469, May 2016, doi: 10.1002/ppul.23380.

[7] A. B. Chang, R. Fortescue, K. Grimwood, E. Alexopoulou, L. Bell, J. Boyd, A. Bush, J. D. Chalmers, A. T. Hill, B. Karadag, F. Midulla, G. B. McCallum, Z. Powell, D. Snijders, W.-J. Song, T. Tonia, C. Wilson, A. Zacharasiewicz, and A. Kantar, "European respiratory society guidelines for the management of children and adolescents with bronchiectasis," *Eur. Respiratory J.*, vol. 58, no. 2, Aug. 2021, Art. no. 2002990, doi: 10.1183/13993003.02990-2020.

[8] N. Kapur, J. P. Masel, D. Watson, I. B. Masters, and A. B. Chang, "Bronchoarterial ratio on high-resolution CT scan of the chest in children without pulmonary pathology," *Chest*, vol. 139, no. 6, pp. 1445–1450, Jun. 2011.

[9] T. L. Badger, "Bronchiectasis; treatment and prevention," *New England J. Med.*, vol. 237, pp. 937–941, Jan. 1947.
[10] W. Finke, "Prospects for prevention of chronic bronchitis and bronchiectasis; rational management of bronchopulmonary infections by penicillin aerosol therapy," *J. Pediatrics*, vol. 33, pp. 29–42, Jul. 1948.
[11] C. E. Field, "Bronchiectasis in childhood: II. Aetiology and pathogenesis, including a survey of 272 cases of doubtful irreversible bronchiectasis," *Pediatrics*, vol. 4, pp. 231–248, Jul. 1949.
[12] E. A. Gaillard, H. Carty, D. Heaf, and R. L. Smyth, "Reversible bronchial dilatation in children: Comparison of serial high-resolution computer tomography scans of the lungs," *Eur. J. Radiol.*, vol. 47, no. 3, pp. 215–220, Sep. 2003.
[13] H. Ouellette, "The signet ring sign," *Radiology*, vol. 212, no. 1, pp. 67–68, Jul. 1999.
[14] A. Brody and A. Chang, "The imaging definition of bronchiectasis in children: Is it time for a change?" *Pediatric Pulmonol.*, vol. 53, no. 1, pp. 6–7, Jan. 2018.
[15] S. Matsuoka, K. Uchiyama, H. Shima, N. Ueno, S. Oish, and Y. Nojiri, "Bronchoarterial ratio and bronchial wall thickness on high-resolution CT in asymptomatic subjects: Correlation with age and smoking," *Amer. J. Roentgenol.*, vol. 180, no. 2, pp. 513–518, Feb. 2003.
[16] T. Fischer, Y. E. Baz, N. Graf, S. Wildermuth, S. Leschka, G.-R. Kleger, U. Pietsch, M. Frischknecht, G. Scanferla, C. Strahm, S. Wälti, T. J. Dietrich, and W. C. Albrich, "Clinical and imaging features of COVID-19-Associated pulmonary aspergillosis," *Diagnostics*, vol. 12, no. 5, p. 1201, May 2022.
[17] V. Goyal and A. B. Chang, "Bronchiectasis in childhood," *Clinics Chest Med.*, vol. 43, no. 1, pp. 71–88, 2022.
[18] L. He, X. Ren, Q. Gao, X. Zhao, B. Yao, and Y. Chao, "The connected-component labeling problem: A review of state-of-the-art algorithms," *Pattern Recognit.*, vol. 70, pp. 25–43, Oct. 2017.
[19] E. W. Weisstein, "Grid graph. From MathWorld—A wolfram web resource," Wolfram Research, Inc., IL, USA, 2012. [Online]. Available: https://mathworld.wolfram.com/GridGraph.html
[20] R. Davies, "Anne chang: A champion of childhood lung health," *Lancet*, vol. 392, no. 10150, p. 811, Sep. 2018.
[21] M. Prasad, A. Sowmya, and P. Wilson, "Automatic detection of bronchial dilatation in HRCT lung images," *J. Digit. Imag.*, vol. 21, no. S1, pp. 148–163, Oct. 2008.
[22] B. L. Odry, A. P. Kiraly, C. L. Novak, D. P. Naidich, and J. F. Lerallut, "An evaluation of automated broncho-arterial ratios for reliable assessment of bronchiectasis," *Proc. SPIE*, vol. 6915, pp. 807–815, Mar. 2008.
[23] Z. Naseri, S. Sherafat, H. Abrishami Moghaddam, M. Modaresi, N. Pak, and F. Zamani, "Semi-automatic methods for airway and adjacent vessel measurement in bronchiectasis patterns in lung HRCT images of cystic fibrosis patients," *J. Digit. Imag.*, vol. 31, no. 5, pp. 727–737, Oct. 2018.
[24] G. G. King, N. L. Müller, K. P. Whittall, Q.-S. Xiang, and P. D. Paré, "An analysis algorithm for measuring airway lumen and wall areas from high-resolution computed tomographic data," *Amer. J. Respiratory Crit. Care Med.*, vol. 161, no. 2, pp. 574–580, Feb. 2000, doi: 10.1164/ajrccm.161.2.9812073.
[25] E. U. Mumcuoglu, J. Prescott, B. N. Baker, B. Clifford, F. Long, R. Castile, and M. N. Gurcan, "Image analysis for cystic fibrosis: Automatic lung airway wall and vessel measurement on CT images," in *Proc. Annu. Int. Conf. IEEE Eng. Med. Biol. Soc.*, Sep. 2009, pp. 3545–3548.
[26] Y. Nakano, S. Muro, H. Sakai, T. Hirai, K. Chin, M. Tsukino, K. Nishimura, H. Itoh, P. D. Paré, J. C. Hogg, and M. Mishima, "Computed tomographic measurements of airway dimensions and emphysema in smokers: Correlation with lung function," *Amer. J. Respiratory Crit. Care Med.*, vol. 162, no. 3, pp. 1102–1108, Sep. 2000, doi: 10.1164/ajrccm.162.3.9907120.
[27] O. Weinheimer, T. Achenbach, C. Bletz, C. Duber, H.-U. Kauczor, and C. P. Heussel, "About objective 3-D analysis of airway geometry in computerized tomography," *IEEE Trans. Med. Imag.*, vol. 27, no. 1, pp. 64–74, Jan. 2008, doi: 10.1109/TMI.2007.902798.
[28] R. S. J. Estépar, G. G. Washko, E. K. Silverman, J. J. Reilly, R. Kikinis, and C. Westin, "Accurate airway wall estimation using phase congruency," in *Proc. Int. Conf. Med. Image Comput. Comput.-Assist. Intervent.* Berlin, Germany: Springer, 2006, pp. 1–10.
[29] O. I. Saba, E. A. Hoffman, and J. M. Reinhardt, "Maximizing quantitative accuracy of lung airway lumen and wall measures obtained from X-ray CT imaging," *J. Appl. Physiol.*, vol. 95, no. 3, pp. 1063–1075, Sep. 2003, doi: 10.1152/japplphysiol.00962.2002.
[30] L. He, Y. Chao, K. Suzuki, and K. Wu, "Fast connected-component labeling," *Pattern Recognit.*, vol. 42, no. 9, pp. 1977–1987, Sep. 2009.
[31] *ACR-STR Practice Parameter for the Performance of High-Resolution Computed Tomography (HRCT) of the Lungs in Adults*, American College of Radiology, Reston, VA, USA, 2019.
[32] S. Rizvi, C. J. Wehrle, and M. A. Law, "Anatomy, thorax, mediastinum superior and great vessels," in *StatPearls [Internet]*. Treasure Island, FL, USA: StatPearls Publishing, Jan. 2022. [Online]. Available: https://www.ncbi.nlm.nih.gov/books/NBK519576/
[33] I. J. C. Hartmann and N. J. Screaton, "Pulmonary circulation and pulmonary thromboembolism," in *Grainger & Allison's Diagnostic Radiology, 2 Volume Set E-Book*, 7th ed. Amsterdam, The Netherlands: Elsevier, 2020. [Online]. Available: https://www.sciencedirect.com/science/article/pii/B9780702033896000228
[34] S. Standring, *Pleura, Lungs, Trachea and Bronchi, Gray's Anatomy E-Book: The Anatomical Basis of Clinical Practice*. Amsterdam, The Netherlands: Elsevier, 2021.
[35] K. Wu, E. Otoo, and K. Suzuki, "Optimizing two-pass connected-component labeling algorithms," *Pattern Anal. Appl.*, vol. 12, no. 2, pp. 117–135, Jun. 2009.
[36] M. Skalski, "Lobar and segmental bronchial anatomy," Case Study. Accessed: Aug. 2023. [Online]. Available: https://doi.org/10.53347/rID-23285
[37] S. Guo, X. Liu, H. Zhang, Q. Lin, L. Xu, C. Shi, Z. Gao, A. Guzzo, and G. Fortino, "Causal knowledge fusion for 3D cross-modality cardiac image segmentation," *Inf. Fusion*, vol. 99, Nov. 2023, Art. no. 101864.
[38] Y. Zhang, Q. Liao, L. Ding, and J. Zhang, "Bridging 2D and 3D segmentation networks for computation-efficient volumetric medical image segmentation: An empirical study of 2.5D solutions," *Computerized Med. Imag. Graph.*, vol. 99, Jul. 2022, Art. no. 102088.
[39] A. Liew and H. Yan, "Current methods in the automatic tissue segmentation of 3D magnetic resonance brain images," *Current Med. Imag. Rev.*, vol. 2, no. 1, pp. 91–103, Feb. 2006.
[40] S. Zhao, X. Wu, B. Chen, and S. Li, "Automatic vertebrae recognition from arbitrary spine MRI images by a category-consistent self-calibration detection framework," *Med. Image Anal.*, vol. 67, Jan. 2021, Art. no. 101826.
[41] J. Jang and D. Hwang, "M3T: Three-dimensional medical image classifier using multi-plane and multi-slice transformer," in *Proc. IEEE/CVF Conf. Comput. Vis. Pattern Recognit. (CVPR)*, Jun. 2022, pp. 20686–20697.
[42] R. Siega, E. J. R. Justino, J. Facon, F. Bortolozzi, and L. R. Aguiar, "Automatic volumetric segmentation of encephalon by combination of axial, coronal, and sagittal planes," *Res. Comput. Sci.*, vol. 147, no. 4, pp. 111–123, Dec. 2018.
[43] S. Zhuang, F. Li, A. N. J. Raj, W. Ding, W. Zhou, and Z. Zhuang, "Automatic segmentation for ultrasound image of carotid intimal-media based on improved superpixel generation algorithm and fractal theory," *Comput. Methods Programs Biomed.*, vol. 205, Jun. 2021, Art. no. 106084.
[44] J. Chen, L. Yang, Y. Zhang, M. Alber, and D. Z. Chen, "Combining fully convolutional and recurrent neural networks for 3D biomedical image segmentation," in *Proc. Adv. Neural Inf. Process. Syst.*, vol. 29, 2016, pp. 3036–3044.
[45] P. Mlynarski, H. Delingette, A. Criminisi, and N. Ayache, "3D convolutional neural networks for tumor segmentation using long-range 2D context," *Computerized Med. Imag. Graph.*, vol. 73, pp. 60–72, Apr. 2019.

ABHIJITH REDDY BEERAVOLU is currently pursuing the Ph.D. degree in biomedical engineering with Charles Darwin University, Casuarina, NT, Australia. His thesis is on "Providing interpretability for diverse medical AI systems." This requires working with real-world medical data encompassing images, videos, clinical records, and text to create diagnostic tools and model-specific interpretability techniques. He aims to improve local and global communities by generating innovative ideas to address real-world challenges.

SAMI AZAM is currently a leading Researcher and a Senior Lecturer with the Faculty of Science and Technology, Charles Darwin University, Casuarina, NT, Australia. He is also actively involved in computer vision, signal processing, artificial intelligence, and biomedical engineering research. He has several publications in peer-reviewed journals and international conference proceedings.

MIRJAM JONKMAN (Member, IEEE) is currently a Lecturer and a Researcher with the Faculty of Science and Technology, Charles Darwin University, Casuarina, NT, Australia. Her research interests include biomedical engineering, signal processing, and the application of computer science to real-life problems.

I. BRENT MASTERS has been a Pediatric Respiratory Physician in Calgary, Canada, and Brisbane, Australia, since 1984. He has been the Head or the Director of Pediatric Respiratory Medicine at major hospitals in Brisbane, since 1987, he has extensive clinical expertise, including outreach work in aboriginal and Torres Strait Island communities. His specializations include flexible bronchoscopy, respiratory teaching, and integrating C.T. and bronchoscopy 3D anatomy. He has trained professionals from nine countries, conducted workshops, and contributed to over 150 peer-reviewed publications. Additionally, he has served as an Advisor and a Committee Member for the Thoracic Society of Australia and New Zealand (TSANZ) and Royal Australasian College of Physicians (RACP) on matters related to pediatric bronchoscopy training. He completed the thoracic medicine training in Melbourne and gained additional experience in Calgary.

RAHUL J. THOMAS is a Respiratory and Sleep Pediatrician with Queensland Children's Hospital, Brisbane. He is also a NHMRC Ph.D. Scholar with the Queensland University of Technology Hospital Foundation, supported by Queensland Hospital Foundation, and the CRE in his field of interest, i.e., large airway diseases, and diagnostic modalities of flexible bronchoscopy and thoracic radiology.

ANNE B. CHANG is currently a Senior Staff Specialist with Queensland Children's Hospital, Brisbane. She leads the Cough and Airways Group, Queensland University of Technology. She is also the Leader of the Child Health Division, Menzies School of Health Research at Darwin, Darwin. She is also a Clinician recognized for her research contributions to evidence-based management and clinical care in pediatric cough, asthma, bronchiectasis, and indigenous child lung health. Her original works include the world's first description of protracted bacterial bronchitis and international multicenter trials involving children with bronchiectasis. She has been a NHMRC Practitioner Fellow, since 2004, and has published over 580 articles. Her primary research interests include undertaking clinical research that improves indigenous health management, cough, and suppurative lung disease in children.

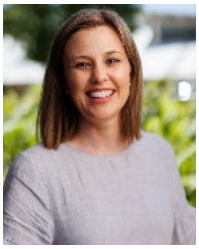

GABRIELLE B. MCCALLUM is currently a Senior Research Fellow, a Senior Lecturer, and the Program Leader of the Child Health Respiratory Team, Menzies School of Health Research at Darwin, Darwin. With a career spanning more than two decades in the NT, USA, she is also dedicating to enhancing clinical outcomes for children susceptible to adverse lung health outcomes, primarily by addressing early and recurrent acute lower respiratory infections. Her approach involves conducting evidence-based research, developing culturally relevant educational materials, and translating research results into meaningful and culturally appropriate outcomes. Her expertise has extended beyond national boundaries, with her contributions recognized nationally and internationally, including in regions, such as New Zealand, Alaska, Malaysia, and Timor-Leste.

FRISO DE BOER is currently a Professor in engineering with the Faculty of Science and Technology, Charles Darwin University, Casuarina, NT, Australia. His research interests include signal processing, biomedical engineering, and mechatronics.